Modeling multilayered wire strands, a strategy based on 3D finite element beam-to-beam contacts - Part I: Model formulation and validation

Sébastien Lalonde[a], Raynald Guilbault[b], Frédéric Légeron[c]

[a] *Université de Sherbrooke, Faculty of Engineering, Department of Civil Engineering, Sherbrooke, Canada*
[b] *École de technologie supérieure, Department of Mechanical Engineering, Montreal, Canada*
[c] *Parsons Corporation, Abu Dhabi, United Arab Emirates*

Abstract

This paper proposes a FE modeling strategy for multilayered strands subjected to multiaxial loads. The approach takes advantage of beam elements and incorporates 3D inter-wire contacts. While reducing mesh sizes, it handles any strand configuration. Comparisons with experimental results validate its precision. The analysis shows that friction forces control the hysteresis and the bending stiffness. The paper develops a multi-level friction coefficient better representing the stick and slip zones, and to account for indentation, the model incorporates a friction orthogonality concept; the axial direction is controlled by adhesion, while the orthogonal direction is associated with adhesion and deformation contributions.

Keywords: Multilayered wire strands, Finite element modeling, Bending loads, Inter-wire contact, Beam-to-beam contact, Frictional contact

1. Introduction

Multilayered helical strands are key components in many engineering structures, such as suspension and cable-stayed bridges, guyed towers, and power transmission lines. Mainly designed to support high axial static forces, strands are also subjected to dynamic transverse loads (such as wind-induced vibrations) generating free cyclic bending. Near restrained terminations, cyclic bending may induce critical fretting damage at inter-wire contact interfaces, consequently affecting cable service life [1,2]. Characterizing and understanding the mechanical behavior of helical strands under multiaxial loading is thus critical for the structural integrity assessment of engineering structures. This paper develops an efficient modeling strategy for multilayered strands submitted to combined axial and bending loads. Although not restricted to, the proposed modeling approach is oriented to the analysis of overhead conductors.

Due to contact interactions between wires, multilayered strands (Fig. 1a) exhibit a variable bending stiffness (EI); as the strand curvature (κ) increases, the wires progressively start to slip on each other, resulting in a significant reduction of the bending stiffness. Therefore, particularly as a result of the anti-symmetricity of the problem [3], formulating a mechanical model of helical strands submitted to multiaxial loads, including bending moments, represents a difficult task.

Several models in the literature address the bending of helical strands. Based on the strand load/deformation configuration in Fig. 1a, different theoretical approaches are proposed using various kinematic assumptions [3]. For example,

Raoof and Hobbs [4] idealized the strand as a series of concentric orthotropic cylinders, each associated with a specific layer and its corresponding mechanical properties. Lanteigne [5] presented a modeling approach in which the strand response is mainly defined from wire axial forces and independent wire bending. Leclair and Costello [6] applied the Love curved rod equilibrium equations to each wire to derive a mechanical model.

The literature also proposes analytical models focusing on local wire aspects. For example, Argatov [7] analyzed the influence of transverse modifications of the wire section associated with Poisson ratio effects and inter-wire contact flattening. The study revealed that for larger lay angles the contact flattening effects dominate the influence of the Poisson ratio. Later Frikha et al. [8] used an asymptotic expansion approach and exploited the translational invariance of single wires to reduce the dimension of the elastic problem brought in by helical strands. They were therefore able to describe the micro stresses resulting from macroscopic loadings. Although, the analytical models developed in these studies provide detailed descriptions of strand response, the presented analyses remained limited to axial loads and neglected inter-wire friction forces.

Some researchers introduced wire slippage by means of the Coulomb friction law, considering interlayer pressure and axial tension difference in contacting wires at given strand curvatures. This procedure results in a stepwise variation of the bending stiffness between two extremes: EI_{max} (no slip, eq. (1.1)) and EI_{min} (full slip, eq. (1.2)) [9]. In eqs. 1.1 and 1.2, E_j, A_j, γ_j and R_j stand for wire j elastic modulus, cross-section area, angular position and corresponding layer radius, respectively, while I_{0j} is the wire moment of inertia (relative to its own axis):

$$EI_{max} = \sum E_j \left(I_{0j} + A_j R_j^2 sin^2 \left(\gamma_j \right) \right) \tag{1.1}$$

$$EI_{min} = \sum E_j I_{0j} \tag{1.2}$$

The EI_{max} assumption considers that all strand wires act together as a solid beam, while EI_{min} supposes independent responses of the wires. In other words EI_{min} supposes that each wire bends about its own axis. Therefore, under this second assumption, straight strands involving no inter-wire slip have a bending stiffness equivalent to that resulting from EI_{max}. On the other hand, with bending deformations, the strand curvature generates inter-wire slippage causing bending stiffness reductions. The EI_{min} condition is reached when the induced curvature produces slipping conditions at all wire contacts.

In the late '90s, Papailiou [10] presented a model in which the friction was also defined by the wire axial tension. The model accounts for the distance from the strand neutral axis, thus leading to a smooth bending stiffness variation between EI_{max} and EI_{min}. To incorporate EI variations along the strand under free bending conditions, the approach was implemented

into a finite element analysis. Comparisons with experimental measures showed good correlations [10]. Subsequently, Hong et al. [11] reconsidered certain hypotheses related to pressure transmission between layers, while Paradis and Legeron [12] extended the representation to include the effects of tangential compliance at contact interfaces.

Despite the good performances more recent models have shown in predicting strand-free bending response, their analytical formulations involve significant simplifications [13]. For instance, contacts between adjacent wires on the same layer are neglected, while contact points of superposed layers are replaced by contact lines. Moreover, under no-slip conditions (EI_{max}), strand cross-sections remain plane after bending (Euler-Bernouilli hypothesis) [11]. The wire torsional stiffness is also neglected. These hypotheses are acceptable for global analyses of strand located far from restrained terminations. However, they may induce significant deviations when evaluating wire stresses close to positions where fatigue damage is a primary concern. Moreover, due to the inherent limitations of closed-form analytic models, considering the effects of restraining fixtures (suspension clamps) and analyses beyond the material linear elastic limits are practically impossible.

To overcome the limitations of analytical models, and mostly as a result of recent advances in numerical methods and computer performance, several authors have proposed full 3D finite element modeling [14–17]. In these numerical studies, each wire of the multilayered strand is discretized with 3D solid elements, where surface-to-surface contact elements simulate all inter-wire contact types. In some cases, the model accounts for plastic deformations by means of nonlinear hardening laws [14,15]. With the ability to characterize local wire stresses without losing the global strand kinematics, 3D FE models appear to be very useful. However, the full 3D solid modelling approaches inevitably generate models leading to high computational cost [14,18]. This in part explains why 3D FE strand models are almost exclusively limited to short-strand-length, and axi-symmetrical loads (axial tension and torsion). Although Zhang et al. [19] successfully analyzed strand bending stiffness using a solid 3D FE model, their study was considering a single layer cable of one pitch length.

In reality, to minimize boundary effects, multilayered strand analysis under free bending conditions would require a model capable of supporting long spans of few pitch length. Unfortunately, current FE models still appear to be inadequate when it comes to efficiently analyzing the free bending of multilayered strands.

This paper develops an intermediate FE modeling approach. The objective is to obtain a precise model eliminating most of the simplifying hypotheses of theoretical models, while remaining computationally affordable. The proposed approach

uses 3D one-dimensional elements known as beam elements, combined to a beam-to-beam contact algorithm to describe wire geometry and contact interactions.

The beam elements strategy has recently been evaluated in some papers [20,21]. Zhou and Tian [21] used beam elements to model a single-layered strand, where the wire contact interactions were managed through coupling equations between correspondent nodes. Inter-wire slippages were therefore not considered, and even though the model was applied to analyses of strands submitted to bending loads, this approach remains limited to single-layered strands under small deflection. In Beleznai et al.'s [20] paper, each inter-wire contact is simulated by spring elements presenting a stiffness derived from Hertz contact theory. Although the accuracy of the approach was demonstrated, the authors acknowledge that it remains limited to one- or two-layered strands submitted to small displacements.

The present paper extends the beam modeling approach to multilayered strands undergoing large deformations and displacements. Although the developed procedure is general and appropriate for any finite element (FE) software, this work uses Ansys®.

2. Finite element modeling approach

2.1. Multilayered wire strand geometry

Generally, wire strands are composed of N helical layers wrapped around a straight central core. Adjacent layers are usually wound in opposite directions to minimize internal moments due to winding effects (Fig. 1b). Each layer i is characterized by the number of wires (n_i), the wire diameter (d_j), its lay angle (α_i) and its layer radius (R_i) given by eq. (2.1):

$$R_i = \frac{d_{core}}{2} + \frac{d_i}{2} + \sum_{k=1}^{k=i-1} d_k \tag{2.1}$$

Since, in the proposed approach, the 3D beam element nodes are located on the wire axis, the whole strand geometry is completely defined by the wire centerlines. For straight cable segments, the wire centerlines are helix curves (Fig. 1c). Following an approach similar to Stanova et al. [16], the helix curve of wire j in a layer i is generated from parameterized equations (eq. (2.2)):,

$$x = R_i cos\left(\gamma_i + \frac{2\pi(j-1)}{n_i} + qt\theta_i\right)$$
$$y = R_i sin\left(\gamma_i + \frac{2\pi(j-1)}{n_i} + qt\theta_i\right) \quad (2.2)$$
$$z = Lt$$

where $t \in [0,1]$, L is the strand length, q determines the right hand ($q = 1$) or left hand ($q = -1$) lay direction, and θ_i is the total rotation i given by $\theta_i = \tan(\alpha_i)L/R_i$. Finally, γ_i is the wire starting angular position (Fig. 1b).

2.2. Geometry discretization

Each wire centerline is discretized using one-dimensional 3D beam elements (Fig. 1c). The BEAM189 elements in Ansys® are composed of three nodes with 6 degrees of freedom (DOF), and use second-order shape functions. The beam element stiffness matrices are defined in the linear elastic domain via the wire radius (r), the material Young modulus (E) and Poisson ratio (υ). In reality, the present work does not integrate the υ effects on the transverse contractions of the wire sections; indeed, Ghoreishi et al. [22] demonstrated that for lay angles (α) below 15° these deformations only have a negligible influence on the global strand behavior. Kumar and Botsis [23] also concluded that υ induces no significant alteration of the contact stress distributions in multilayered strands.

As illustrated in Fig. 1c, the beam elements reduce the mesh size by 2 orders as compared to 3D solid modeling. Obviously, this approach cannot account for local form deviations. However, based on St-Venant principle, it may be considered that these local effects should not affect the macroscopic behavior of the global wire strand.

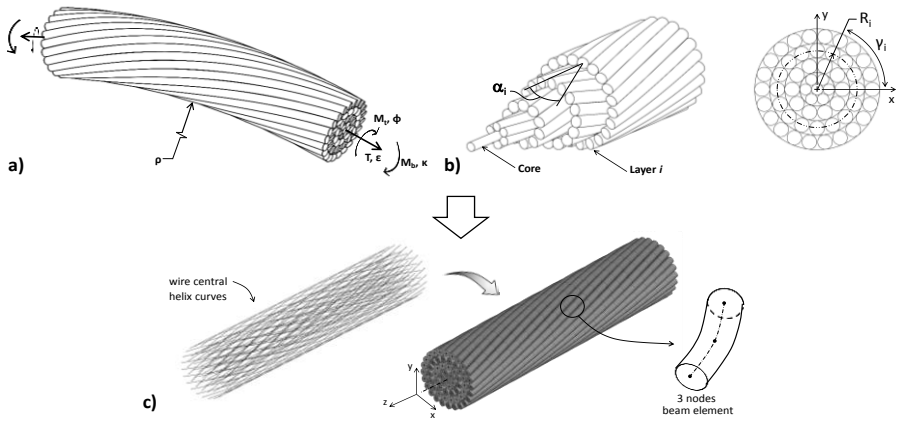

Fig. 1 – Wire strand load/deformation configuration (a), geometric configuration (b) and FE model using beam elements (c)

2.3. Inter-wire contact modeling

Interactions between wires represent one of the key aspects of wire strand characterization. Two types of contacts can be found in a strand: 1- Lateral contacts (Fig. 2a) correspond to the interactions between wires of the same layer, while 2- Radial contacts associate wires of adjacent layers (Fig. 2b). Contacts between the central core and adjacent layers belong to the Lateral contact category.

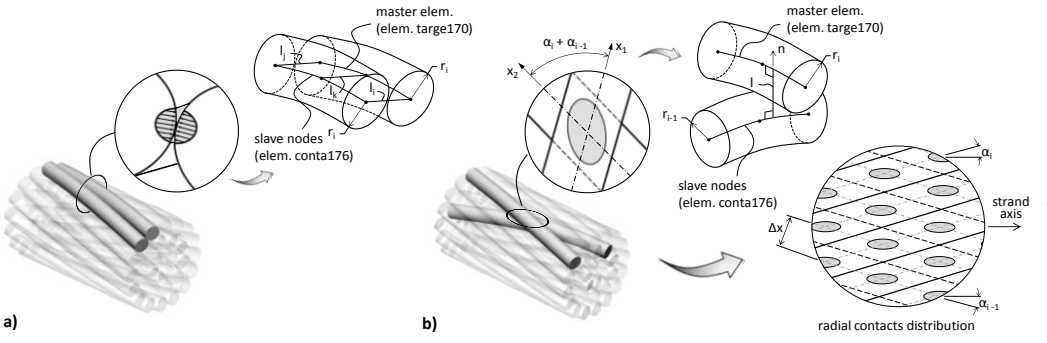

Fig. 2 – (a) Lateral contact line and (b) radial contact point with 3D beam-to-beam contact configuration

A line-to-line contact approach using one-dimensional 3D master/slave element contact pairs, mapped onto beam elements (Fig. 2) is employed for both inter-wire contact types. In Ansys®, contact elements CONTA176 and TARGE170 constitute the slave and master elements, respectively. For radial contacts, CONTA176 elements are mapped onto beams of the inner layer, while TARGE170 elements are associated with the elements of the second layer. The occurrence of contact between two beam elements is determined using a gap function (g_n) (eq. (2.3)); contact interactions are established when $g_n \leq 0$:

$$g_n = l - \left(r_i + r_{i+1}\right) \tag{2.3}$$

In eq. (2.3), *l* represents the normal distance between the centerline of contacting beam elements (Fig. 2(a)). Moreover, since the line-to-line contact algorithm integrated in the present solution neglects the wire flattening and radial contraction contributions, the wire cross-sections are assumed to have constant radii r_i and r_{i+1}.

For parallel wires (Lateral contact), contact conditions (open or closed) are verified at each contact node, while for crossing wires (Radial contact), the conditions are evaluated all along the length of the beam elements. In the present model, each inter-wire contact is individually defined by a set of master/slave element pairs. For lateral contact, all the beam elements associated with the considered wires are included in the contact pair. On the other hand, for radial contacts, only elements near the contact point are examined. To select the proper beam elements, the location of each radial contact point (illustrated in Fig. 2b) is estimated using the relation defined by eq. (2.4) [24]:

$$\Delta x \approx \frac{2\pi R_{ct}}{n_{i-1}} \cdot \frac{cos(\alpha_{i-1})}{sin(\alpha_i + \alpha_{i-1})} \quad (2.4)$$

where R_{ct} is the contact radius between layers i and i-1, given by $R_{ct} = R_i - d_i/2 = R_{i-1} + d_{i-1}/2$.

The proposed model also accounts for friction at inter-wire contacts. Based on Coulomb frictional law, when juxtaposing normal (P) and tangential (Q) inter-wire contact forces obtained from the FE solution, the wires are assumed to be under stick conditions when $|Q| \leq \mu P$ and to start slipping when $|Q|$ reaches μP. Thus, under the sticking condition no relative tangential wire displacement is allowed at the contact interface. On the other hand, under the sliding condition the contacting wires slide on each other and $|Q|$ is set to μP.

While various contact algorithms are available for modeling contact pairs, the penalty method is preferred because of the large number of inter-wire contacts involved, and because it does not add any DOF to the equation system. The penalty algorithm uses a normal (K_n) and tangential (K_t) contact stiffnesses in order to minimize the penetration (δ_n) and prevent relative sliding (δ_t) in stick conditions at the contact and interface. Ansys® defines these parameters with the following semi-empirical expressions (eq. (2.5) and eq. (2.6)):

$$K_n = f_{K_n} \cdot E \cdot d \cdot \xi_n \quad (2.5)$$

$$K_t = \frac{f_{K_t} \cdot \mu \cdot E \cdot d^2 \cdot \xi_t}{h} \quad (2.6)$$

where in eq.(2.5) f_{Kn} is a normal stiffness factor, d the beam element diameter, and ξ_n a multiplying factor whose default value is set to 10. In eq. (2.6) f_{Kt} is a tangential stiffness factor, h the contact element size, and ξ_t a multiplying factor set to 3.75 by default. Values of 1.0 and 50.0 for f_{Kn} and f_{Kt} respectively, have proven to give results comparable to the Lagrangian contact algorithm commonly considered as theoretically exact.

2.4. Boundary conditions and loading application

In order to prevent any wire unwinding displacement, the ends of the strand are considered as rigid planes. Thus, all nodes located at one strand extremity are fully coupled to the node located at the central core by constraint equations. The end boundary conditions (traction force, imposed extension or displacement constraints) are thus applied only at the central core nodes.

2.5. Model solution

The wire strand model solution makes use of a direct sparse solver, combined to a Newton-Raphson algorithm to deal with large displacements, contacts and material nonlinearities. Force and moment equilibrium are verified at each solving iteration where convergence is assumed when the L2 norm residual is less than 0.5%. All simulations presented in this paper were realized on a 2.9 GHz quad-core CPU with 12 GB of RAM.

3. Model validation

This section establishes the precision of the proposed approach. Results of published studies are compared to values obtained from the present model.

3.1. Wire strand analysis under axial loading

Fig. 3 shows the first examined configuration, where the wire strand is submitted to an axial tension load *T*.

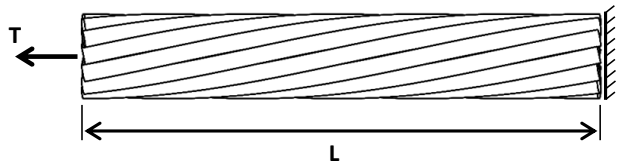

Fig. 3 - Wire strand cable under axial loading

This first analysis considers the 7-wire single layer strand studied experimentally by Utting and Jones [25]. Table 1 presents the geometric and mechanical properties of the strand. Judge et al. [14] recently modeled the same configuration using a full 3D FE model made of linear solid elements. The following comparison includes the results of both publications.

Table 1 - Properties of 7-wire strand

Layer	n_i	d_i (mm)	E (GPa)	υ	E_t (GPa)	σ_y (MPa)	α_i (°)
Core	1	3.94	188	0.3	24.6	1540	-
1	6	3.73	188	0.3	24.6	1540	11.8

In the present case, the strand is loaded beyond its elastic limit. The material plasticity is introduced with a bilinear kinematic hardening law using the material yield point (σ_y) and tangent modulus (E_t) given in Table 1. As proposed by Judge et al. [14] the cable model integrates a strand length (L) of 200 mm. The constituent wires are discretized with beam elements with an average length of 10 mm. Preparatory simulations not included here showed good convergence/CPU time ratios with this mesh definition for the wire diameter (d_j) ranging between 3 and 5 mm. This element size is thus used for all following simulations. The 7-wire single layer strand mesh includes 168 beam elements, 288 contact pairs and 343 nodes.

Compared to the 147,000 solid elements and 163,212 nodes of the full 3D reference model [14], the proposed approach offers an obvious mesh size reduction. Although not specified in the work of Utting and Jones [25], Judge et al. [14] applied a friction coefficient μ of 0.115 to all contact points. The present simulation uses the same coefficient value.

The strand analysis integrates fixed and free end boundary conditions. The fixed end condition only admits axial extensions, while the free end one also permits rotation about the strand axis. Fig. 4 compares the calculated axial load/deformation results to the published experimental and numerical values.

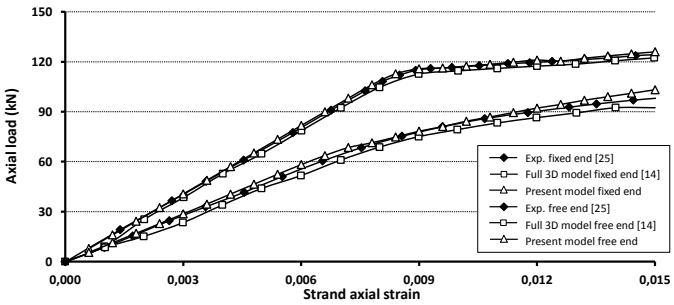

Fig. 4 - Axial strain vs. axial load for the 7-wire strand

Fig. 4 shows the high correspondence between the results established with the proposed modeling strategy and those published in the references.

The same case study was also modeled by Jiang and Henshall [26]. Exploiting the cyclic symmetry of the strand, the authors developed a refined 3D FE model including only one wire and the contacting core sector. This approach produced detailed information on the contact stresses. Table 2 compares the inter-wire contact forces per unit of length (*p*) extracted from the present model to those presented by Jiang and Henshall [26]. The table indicates that the overall correspondence is higher than 93%.

Table 2 – Core-wire contact force comparison

Axial Strain (ε)	p (N/mm) Ref. [26]	p (N/mm) Present model	Diff. (%)
0.002	40.3	43.0	6.6
0.004	80.8	85.9	6.2
0.006	120.8	127.9	5.9
0.008	160.4	169.9	5.9
0.010	178.7	185.3	3.7
0.012	184.7	189.9	2.8

In addition to the 7-wire strand, Judge et al. [14] also examined a 120-wire multilayered steel strand. Table 3 gives the 120-wire strand properties taken from the reference paper. The authors of the paper established the tangent modulus E_t from the wire axial stress/deformation chart [27].

Fig. 5a shows the stress distribution established with the present model, while Fig. 5b compares the axial load/deformation results to the values published by Judge et al. [14]. The graph in Fig. 5b also includes experimental data measured on a 6m cable specimen [14]. The reference document [27] indicates that the model solution lasted 12 hours on a desktop computer equipped with quad-core CPU and 32 GB of RAM.

Table 3 - Properties of 120-wire multilayered strand

Layer	n_i	d_i (mm)	E (GPa)	υ	E_t (GPa)	σ_y (MPa)	α_i (°)
Core	1	5.8	188	0.3	5.5	1540	-
1	7	4.3	188	0.3	5.5	1540	11.94
2	17	3.2	188	0.3	5.5	1540	14.75
3	14	5.3	188	0.3	5.5	1540	14.37
4	21	5.0	188	0.3	5.5	1540	15.23
5	27	5.0	188	0.3	5.5	1540	15.66
6	33	5.0	188	0.3	5.5	1540	15.95

The full 3D model required 2,520,000 solid elements and 2,797,920 nodes for a length *L* equal to 200 mm [14]. On the other hand, the present approach led to a mesh size of 2640 beam elements, 5869 contact pairs, 5400 nodes and a 62-minute solution.

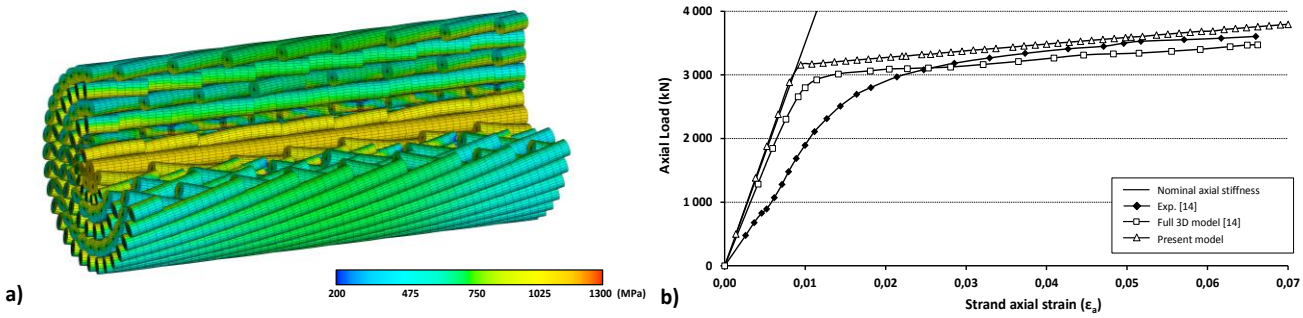

Fig. 5 - 120-wire strand partial view of Von Mises stress (σ_{VM}) distribution at (a) ε_a = 0.0056 and (b) axial strain (ε_a) vs. axial load

Although the numerical solutions significantly deviate from the experimental measures for the elastic domain part, Fig. 5b shows that both models produce valuable and similar predictions of the theoretical cable stiffness. Judge et al. did not explain the experimental/numerical differences.

These first results show that, while considerably reducing the mesh size, the proposed beam modeling strategy offers descriptions of the global behavior of axially loaded strand cables with a precision equivalent to that provided by significantly more sophisticated models, and even extends beyond the elastic limit.

3.2. Strand response under combined axial/bending loads

This second series of validation analyses combines bending forces and axial loadings. Fig. 6 illustrates the cable load arrangement. This configuration corresponds to the experimental bending tests conducted by Papailiou [10,28], where a transverse load *V* varying between 0 and V_{max} is applied at the midspan position (z = 0 mm), while the wire strand is maintained at a specified tension value *T*, using rigid clamps. These clamps virtually prevented any cable slippage at both ends.

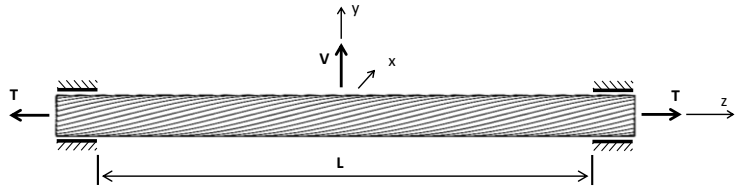

Fig. 6 - Wire strand cable under axial and bending loading

In his work, Papailiou [28] analyzed two multilayered strands: 1- a S32 steel cable (Table 4) and 2- a ACSR Cardinal electrical conductor (Table 5). ACSR strands consist of a steel core and layers of aluminum wires. Both cable specimens were 1.0 m long.

Table 4 - Properties of S32 cable

Layer Nb.	Wire Nb.	Wire d_j (mm)	E (GPa)	υ	α (°)
Core	1	3.72	200	0.3	-
1	6	3.54	180	0.3	14.22
2	12	3.54	180	0.3	13.69
3	18	3.54	180	0.3	13.99
4	24	3.54	180	0.3	13.97

Table 5 - Properties of Cardinal ACSR conductor

Layer Nb.	Wire Nb.	Wire d_j (mm)	E (GPa)	υ	α (°)
Core	1	3.34	210	0.3	-
1	6	3.34	180	0.3	6.06
2	12	3.32	65	0.33	11.99
3	18	3.32	65	0.33	11.80
4	24	3.32	65	0.33	13.10

The following section examines the S32 cable. The present analysis assumes a linear elastic behavior, and imposes a constant coefficient of friction μ_a equal to 0.3 for all inter-wire contacts. This value is derived from friction force measurements published by Papailiou [28]. The DOF of both cable ends are constrained and only admit displacements in the axial direction. In addition, to prevent any rigid body movement, one core node located at the cable midspan (z = 0 mm) is axially constrained. The modeled cable length is *L* = 1000 mm. This length corresponds to the reference experimental test setup [10].

During the first load steps, the tension force T is applied in 20-load increments, and thereafter maintained for the rest of the simulation. After that, the transversal load V is also incrementally applied. After reaching the V_{max} value, the transversal load is gradually brought back to 0 following the inverse 20-load steps. This load sequence was repeated for a few load cycles, with T = 280 kN and V_{max} = 40 kN.

The numerical tests indicated that, using this load configuration, the cable load/deflection hysteresis reaches a steady-state regime at the second load cycle.

Fig. 7a shows the strand deformation and corresponding von Mises stress distributions after two load cycles, while Fig. 7b presents the resulting midspan load-deflection curve. The graph of Fig. 7b also includes Papailiou's experimental measurements and the theoretical evaluations made with eq. (3.1), considering EI_{max} and EI_{min}.

In eq. 3.1, $k = (EI/T)^{½}$ and $s = L/4$. Integrating the S32 cable properties given in Table 4 into eqs. 1.1 and 1.2 leads to 6357.8 Nm² and 82.7 Nm² for EI_{max} and EI_{min}, respectively.

The experimental and theoretical evaluations presented in Fig. 7 have been shifted to have their origins correspond to the x-intercept of the steady-state hysteresis.

$$y_{max} = \frac{Vk}{T}\left[\frac{L}{4k} - \frac{1-e^{-L/2k}}{1+e^{-L/2k}}\right] \qquad (3.1)$$

While the chart shows a good correlation between the model predictions and the experimental data, the large hysteresis areas indicate that the simulations overestimate the friction losses.

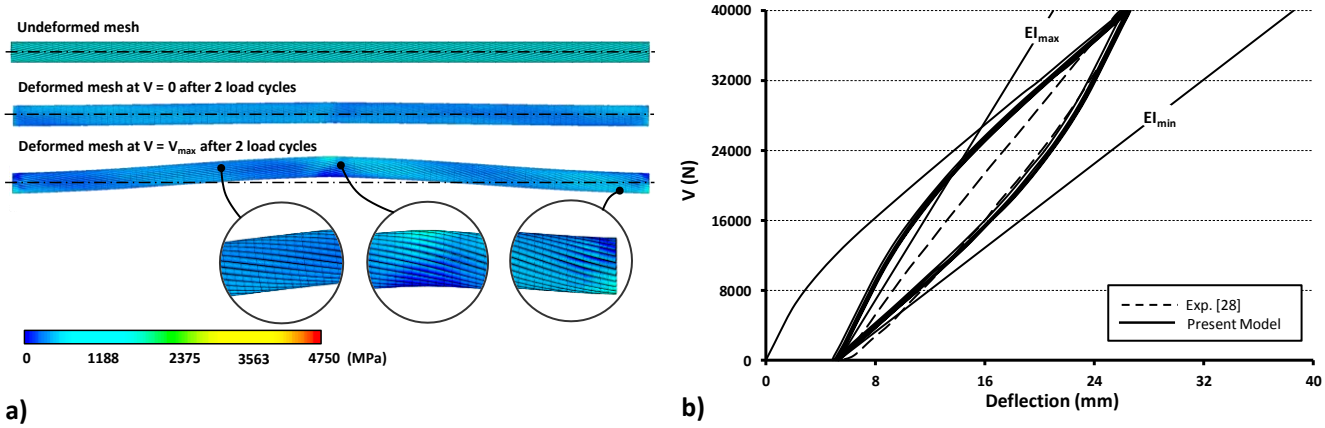

Fig. 7 - S32 cable (T = 280 kN and V_{max} = 40 kN), Von Mises stress (σ_{VM}) distributions after (a) 2 load cycles and (b) 5 cycle load-deflection hysteresis curve at the cable center (Z = 0 mm), V variation between 0 and V_{max}

The following simulations consider four load configurations (T;V_{max}) given in kN: Case 1 (40;5), Case 2 (80;10), Case 3 (140;20) and Case 4 (280;40). Fig. 8 compares the cable deflection over a 150 mm distance to the experimental results

presented by Papailiou for $V = V_{max}$. The numerical deflection values are evaluated at the nodes defining the central core wire. Moreover, in order to illustrate the wire slippage effect, the graph of Fig. 8 also includes the theoretical cable deflection curves calculated with eq. 3.2 [29], considering the EI_{max} and EI_{min} assumptions.

$$y(x) = \frac{Vk}{2T}\left[\left(\sinh\left(\frac{x}{k}\right) - \frac{x}{k}\right) - \tanh\left(\frac{s}{k}\right)\left(\cosh\left(\frac{x}{k}\right) - 1\right)\right] \tag{3.2}$$

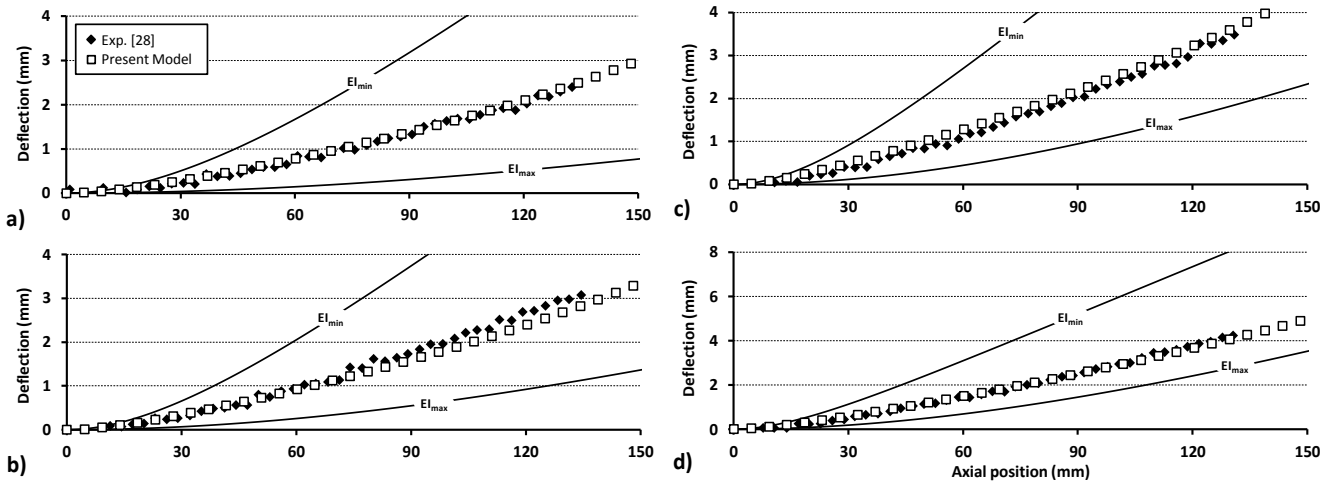

Fig. 8 - S32 cable deflection a) Case 1, b) Case 2, c) Case 3 and d) Case 4

The numerical solutions presented in Fig. 8 demonstrate a perfect correspondence with the experimental data. Fig. 8 also illustrates the imprecision associated with the theoretical expression (eq. 3.2). The inaccuracy associated with eqs. 1.1 and 1.2 is also visible in Fig. 7b) with y_{max}.

The following analyses examine the ACSR Cardinal conductor described in Table 5. Compared to the previous simulation, the friction coefficient is changed to $\mu_a = 0.5$ to describe the aluminum-aluminum and steel-aluminum contacts, while $\mu_a = 0.3$ remains at the steel-steel wire contacts.

The simulations only include one load case: T = 40 kN and V_{max} = 4.3 kN. Fig. 9a) and b) present the cable deflection at V_{max} and the midspan (z = 0 mm) load-deflection response, respectively. For clarity, the simulation results established for the first transversal load application have been removed from Fig. 9b), while the remaining part is moved to have its x-intercept at x = 0. Both graphs also include the Papailiou experimental data and the theoretical curves established with EI_{max} = 1800.4 Nm² and EI_{min} = 28.3 Nm² (eqs. 1.1 and 1.2).

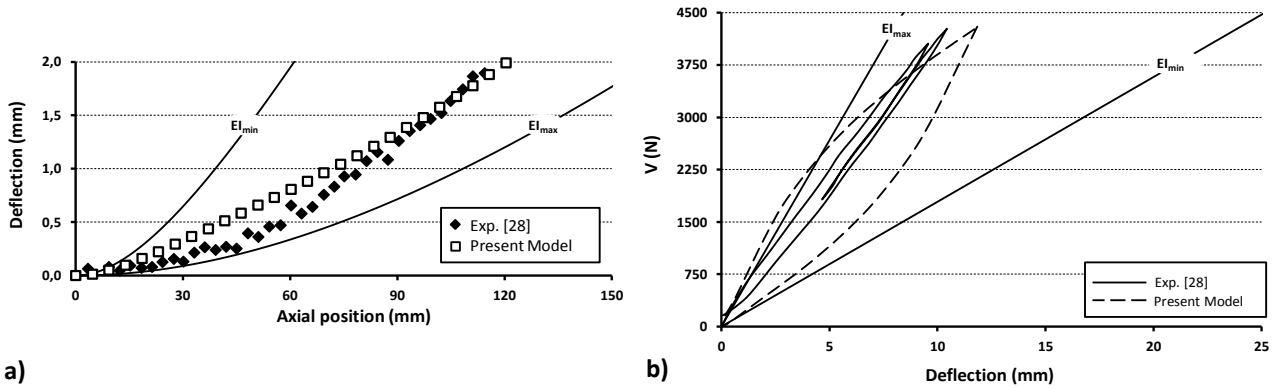

Fig. 9 - ACSR cardinal (T = 40 kN and V_{max} = 4.3 kN), (a) deflection and (b) load-deflection curve at the cable center (Z = 0 mm), V variations between 0 and V_{max}

The V_{max} deflection comparison once again shows good agreement between the numerical results and the experimental values (Fig. 9a), while the predicted hysteresis area remains larger than the measured response (Fig. 9b).

Despite the differences noted, the simulation results show that the proposed modeling approach is adapted to multilayered strand simulation; the model accurately reproduces the nonlinear cable response, which is largely controlled by friction forces at the inter-wire contacts.

4. Analysis of the wire strand under combined axial/bending loads

Although the model capacity to simulate strands submitted to complex loadings was confirmed in the previous section, the differences revealed for the ACSR Cardinal case require additional attention. The following reconsiders the ACSR Cardinal response, and presents a deeper analysis of the Section 3.2 simulation results.

4.1 Distribution of inter-layer contact interaction

Levesque et al. [30] conducted vibration tests on an ASCR Bersfort conductor clamped with fixtures similar to those considered in Papailiou's research. The tests were conducted with induced vibrations producing deflection amplitudes (Δy) of 0.3 mm at 89 mm (3.5 in) from the clamp edge. The authors reported contact point statuses from the first 250mm conductor segment outside the clamp (-500 to -250mm) at layer interfaces 2-3 and 3-4 (see Fig. 12). They mapped the contact conditions according to three statuses: A - Sticking, B – Sliding, and C - Slipping (partial relative displacements). Fig. 10 schematically reproduces the reference observations mapped onto the strand.

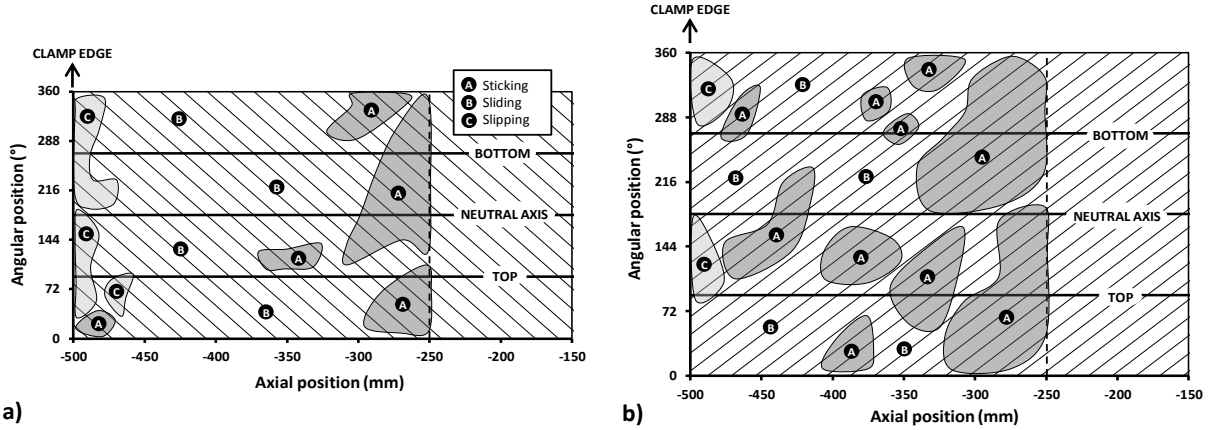

Fig. 10 - ACSR Bersfort conductor, mapping of contact points status between (a) layers 2 and 3 and (b) between layers 3 and 4 (reproduced from Levesque et al. [30] **)**

To assess the validity of the inter-wire contact description obtained from the present model, Fig. 11 presents the model predictions obtained for the ACSR Cardinal conductor defined in Table 5, using a similar mapping approach. In order to have deflection amplitudes comparable to the Levesque et al. [30] test conditions, the tests were conducted with $V = 0.4V_{max}$ (V_{max} = 4.3 kN).

The reference results [30] also revealed slipping marks at the conductor/clamp interface from the clamp edge, up to 22 mm inside the clamped zone. In the present model, the node coupling at the conductor ends (equivalent to clamping edges) prevents any relative motion, and can be considered as the limit point of contact slip observed in the reference [30]. Hence, the contact point statuses predicted by the model are mapped in Fig. 11, considering the clamp edge positioned at -478mm (22 mm from the restrained end). Finally, since the model formulation only detects sticking and sliding conditions, and cannot directly describe partial slip, slipping condition occurrences are identified at contact points experiencing a contact status change from sticking to sliding during the V loading process from 0 to $0.4.V_{max}$.

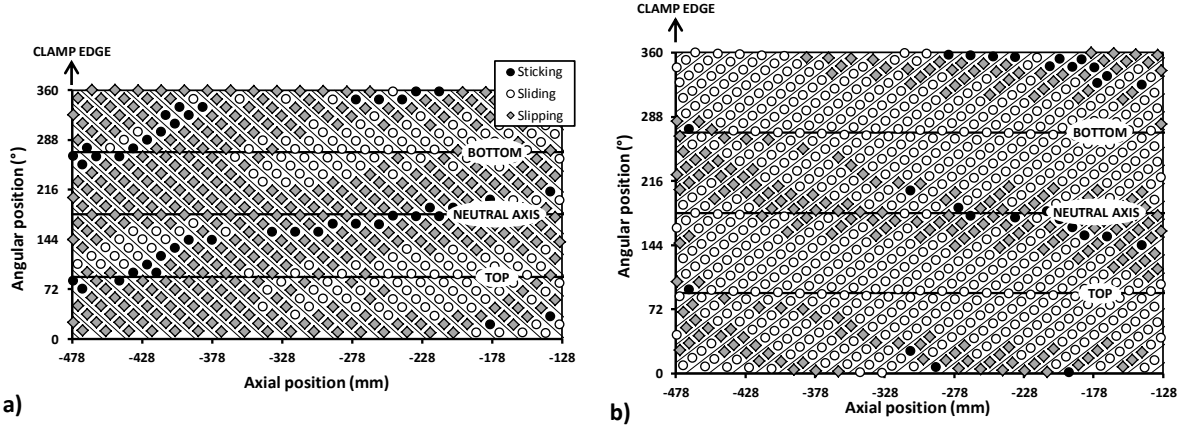

Fig. 11 - ACSR Cardinal at $V = 0.4V_{max}$, mapping of contact points status (a) between layers 2 and 3 and (b) between layers 3 and 4

A comparison of the numerical results (Fig. 11) to the experimental measures (Fig. 10) shows close similarities, despite the differences between the configurations. Indeed, as indicated in the reference descriptions, the predicted contact mappings show that a majority of the points are under sliding conditions, while sticking and slipping zones tend to concentrate close to the evaluation zone limit (axial position -250 mm) and the clamp edge (axial position -500 mm), respectively. The model produces more slipping points at the layer 2-3 contact interface. However, considering the numerical slipping criterion, some of these contact points would probably have been considered under sliding conditions in the experimental description. Globally, the model establishes interlayer contact interactions which are representative of published experimental observations.

4.2 - Wire axial force analysis

The simulation results presented in Fig. 9 (strand deflection and hysteresis) may also be interpreted through wire axial force (F) distributions. Fig. 13 presents the axial force (F) calculated for the nodes of layers 2 to 4 when $V = V_{max}$ (V_{max} = 4.3 kN). Fig. 13 also includes the axial force variation (ΔF) established between V = 0 and $V = V_{max}$. Moreover, for clarity, the graphs only include the predictions made for the more descriptive nodes. These nodes are in the regions near the vertical (top and bottom) and horizontal planes shown in Fig. 12. In addition, since the predictions are symmetrical with respect to the central axial position (z = 0 in Fig. 6), the graph only includes the conductor half-length results. The charts also incorporate the deflection curve established when $V = V_{max}$. For all cases, T was fixed at 40 kN.

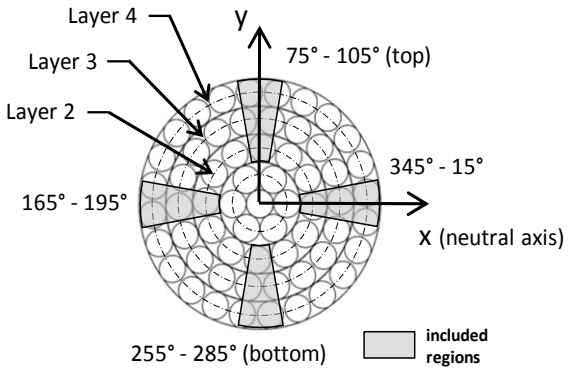

Fig. 12 – Analyzed conductor layers near vertical and horizontal planes (grayed zones)

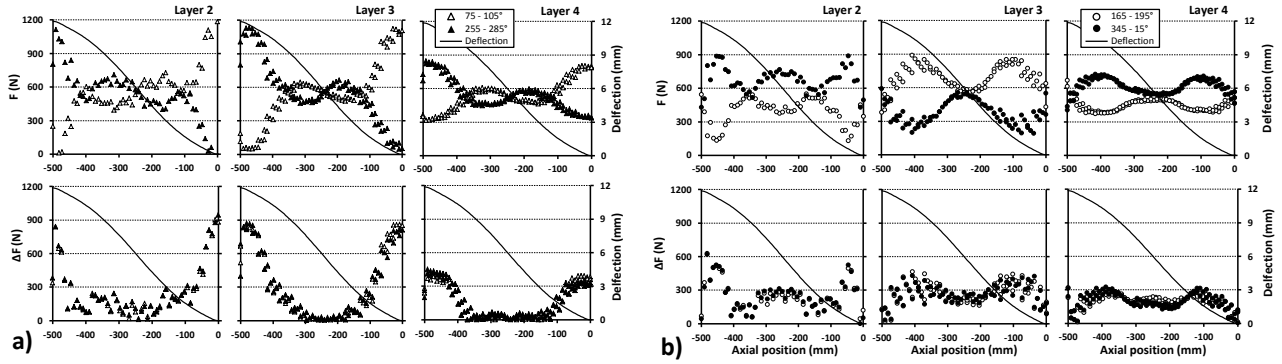

Fig. 13 - Distributions of F when V=V_{max} and ΔF for wires of layers 2, 3 and 4 located near the (a) vertical and (b) horizontal planes

Fig. 13(a) shows that the wires close to the vertical plane experience their maximum F and ΔF values at the V load application points (z = 0mm) and at the clamped end points (z = -500 mm). The charts also indicate that the inner layers support the highest values. F and ΔF are at their minimum amplitude in the straight cable portion (between -150 and -350 mm). On the other hand, the wires close to the horizontal plane (Fig. 13b) mainly sustain the axial force peaks in areas between 50 and 100 mm from the mid (z = 0mm) and end (z = 500mm) cable positions. However, the maximum force values remain significantly lower than those close to the vertical plane. Regarding ΔF, the horizontal plane presents a more uniform distribution, although the maximum variations of ΔF remain located at the positions of the force maxima.

Because of the strand structure (Fig. 1b), an axial tension provokes tightening displacements of the wires, increasing the contact pressure transmitted to underlying layers. Therefore, the high values of F revealed in Fig. 13a explain in part the sticking statuses observed in Fig. 11 close to the clamp edge location at the top and bottom angular positions (90 and 270 degrees). On the other hand, comparing the axial force distribution in the horizontal plane zone angular positions to the contact mappings of Fig. 11 (0-360 and 180 degrees) shows that the highest F/ΔF values are also associated with sticking conditions: between -400 and -128 mm for layer 2-3 contacts and between -328 and -128 mm for layer 3-4 contacts.

4.2 Inter-wire force analysis

The friction wear at a given contact position depends on the local normal force and on the associated sliding distance. This section analyzes the normal force (P), the tangential force (Q) and the slip distance (δ) at selected contact points for the 1-2, 2-3 and 3-4 layer combinations. Fig. 14 presents the simulation results at the positions close to the vertical and horizontal planes shown in Fig. 12. The plots of Fig. 14 also include Δ evaluations made between V = 0 and V = V_{max}. Once again, V_{max} was 4.3 kN, while the axial tension was kept constant at T = 40 kN.

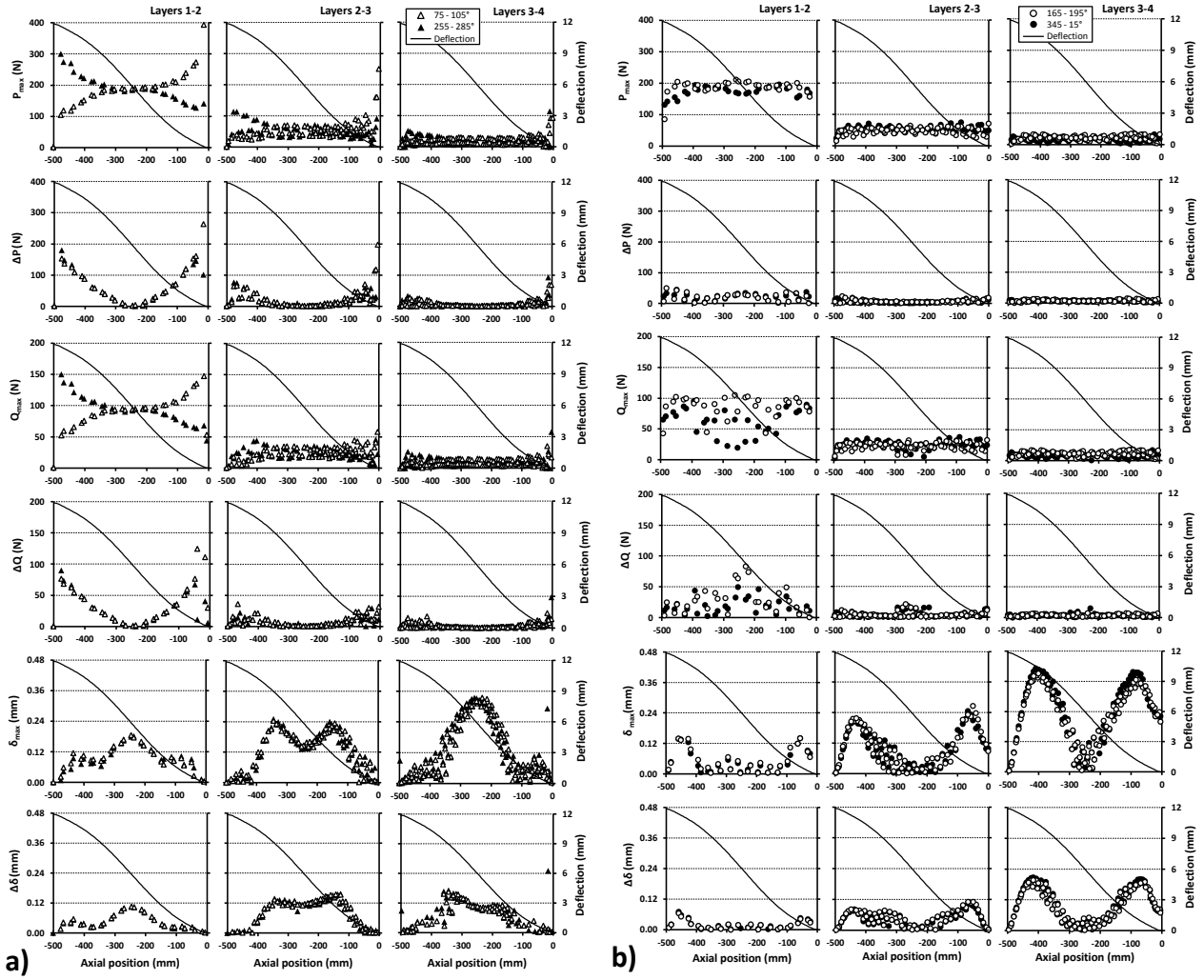

Fig. 14 - Distributions of P when $V=V_{max}$, ΔP, Q when $V=V_{max}$, ΔQ, δ when $V=V_{max}$ and Δδ for contact points located near the vertical (a) and horizontal (b) planes at layer interfaces 1-2, 2-3 and 3-4

Fig. 14a) and b) show that, regardless of the horizontal or vertical region considered, the normal (P, ΔP) and tangential (Q, ΔQ) forces are higher at inter-layer 1-2 than at interlayer 2-3 or 3-4.

The normal/tangential force combinations generate almost inversely proportional slip displacement δ. For example, Fig. 14a shows, for all inter-layer combinations, that the δ predictions remain at low amplitudes for the first 100 mm from the V application point (z = 0 mm) and from the clamp edge position (z = 500 mm). On the other hand, the maximum δ values appear in the 100 to 400 mm portion of the strand; the external layer combination 3-4 show its maximum sliding displacement at 250 mm, which correspond to an inflection point in the conductor deflection curve.

The displacement results presented in Fig. 14b for the horizontal plane region show that δ is also minimal at the clamped end, but significant at the V load position. The maximum slip amplitudes are located in the 50-100 mm and 400-450 mm regions, for all three analyzed inter-layers. Globally, compared to the Fig. 14a results, the δ evaluations presented in Fig. 14b

400 demonstrate practically inverse amplitude distributions along the strand. Based on the force F, P and Q evaluations, as well
401 as on the slip displacement δ predictions, it may logically be concluded that the wire bulk stress and contact conditions
402 present significant fluctuations along the strand, and that the internal layers are submitted to more severe loading
403 conditions.

404 In addition to the surface wear, the normal force P may also cause immediate plastic contact deformations, and influence
405 the coefficient of friction; normal force augmentation increases real contact areas and, consequently, the associated
406 adhesion coefficient of friction (μ_a) as well. The tangential force Q and the slip displacement δ also influence the real contact
407 areas and the adhesion coefficient of friction. Therefore, the significant P, Q and δ variations are good indications that the
408 coefficients of friction are not uniform and constant as assumed within the previous simulations. The next section further
409 investigates how the coefficient of friction influences the simulation results.

410

411 **5. Friction coefficient influence evaluation**

412 Following the previous observations, this section evaluates the effect of different friction modeling approaches.

413

414 *5.1 Friction coefficient magnitude effect*

415 The influence of μ_a is first analyzed considering three values for μ_a at the wire aluminum-aluminum contacts: 0.5, 0.7 and
416 0.9. These coefficients remain similar to the Wharton et al. [31] and Papailiou [10] observations made during experimental
417 fretting/friction tests on aluminum alloy specimens. The contacts involving steel wires remain unchanged and fixed to the
418 values indicated in Section 3.2: μ_a = 0.3 and 0.5 for the steel-steel and steel-aluminum contacts, respectively. Fig. 15
419 compares the results, and illustrates the influence of μ_a on the calculated bending deflection.

420 Fig. 15a) particularly shows that increasing μ_a reduces the deflection slope. Fig. 15b) shows that the high μ_a and low V
421 combinations lead to higher bending rigidities (EI) than the theoretical upper limit EI_{max}. In reality, the same response may
422 have been produced with the introduction of a higher tangential stiffness (K_t). In other words, a change in the inter-layer
423 friction coefficient may generate a corresponding effect on the bending stiffness.

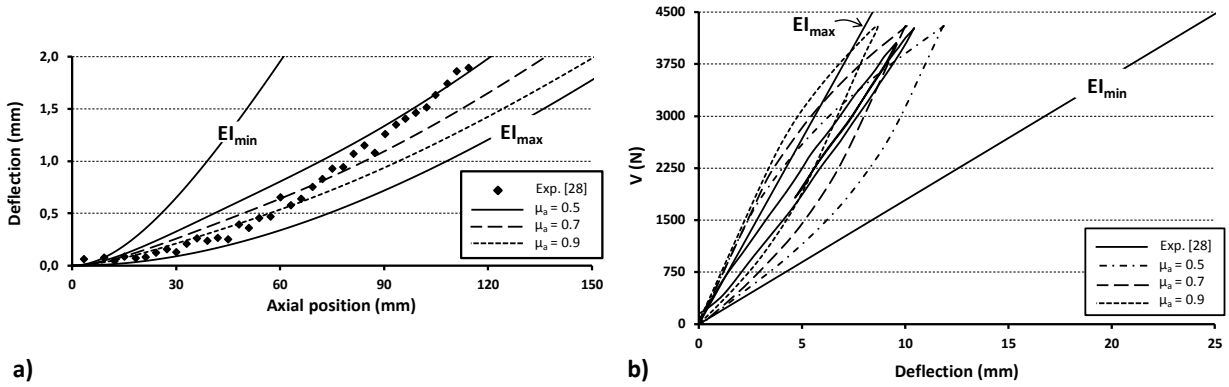

Fig. 15 - ACSR Cardinal (T = 40 kN and V_{max} = 4.3 kN), (a) deflection and (b) load-deflection curve at the cable center (z = 0 mm) V variations between 0 and V_{max} with different values of μ_a

The experimental deflection curve shows that close to the V application point (z = 0 mm), the strand deformation presents a lower gradient than at more distant points, suggesting therefore a reduction of the friction coefficient with an augmentation of the distance from the V application point; for *z* between 0 and 60 mm, the response obtained with μ_a = 0.9 is closer to the measurements, whereas for the remaining part (*z* between 60 and 120 mm), μ_a = 0.5 offers a better correspondence. Actually, the experimental result trend remains close to the theoretical approximation EI_{max} up to a distance of 45 mm from the V application point. On the other hand, at greater distances, the experimental deflection never reaches the EI_{min} prediction. In other words, the Papailiou results suggest that the friction behavior remains close to a no-slip condition around the transversal load application point, and progresses toward sliding conditions, while never attaining a full slip state. Since this behavior does dominate the response in the graphs of Fig. 8 (S32 steel cable), it may be assumed that it is mainly controlled by a combination of elastic and plastic localized deformations of the aluminum wires.

The hysteresis curves in Fig. 15b indicate that higher values of μ_a lead to slightly reduced friction losses since more contact points remain under stick conditions. This observation also advocates for high values of μ_a in the vicinity of the *V* application.

Finally, this analysis indicates that the model should offer an improved precision with friction coefficients better reflecting the variable inter-wire relative displacements along the strand axial position.

5.2 Variable adhesion friction coefficient effect

Considering the mechanical properties of ACSR aluminum wire, it may reasonably be assumed that the loads (P, Q) shown in Section 4 can generate wear and plastic deformations. Fig. 18a shows indentation marks observed on experimental specimens of 19/54 ACSR Géant conductor, similar observations are reported by Azevedo et al. [32]. Altered wire surface

conditions have a direct effect on inter-wire contact. The influence of wire surface changes may be integrated into variable friction coefficient values. However, predicting the complete distribution of μ along the strand remains an impractical endeavor. The following section examines the response quality improvement resulting from a multi-level adhesion coefficient of friction.

In order to force the quasi no-slip condition noted in the V load application point neighborhood and near the clamped ends, a μ_a value of 0.7, equivalent to a static coefficient, is imposed at aluminum-aluminum and aluminum-steel radial contacts over 100 mm (L_{stick}) from the V application point (z = 0 mm) and from the strand fixed extremities (z = 500 mm). On the other hand, slip conditions are promoted with a value equivalent to a dynamic coefficient of friction μ_a = 0.3. This coefficient is applied at the aluminum-aluminum and aluminum-steel radial contacts over four 50 mm strand segments (L_{slip}) next to the no-slip zone. Fig. 16 shows the proposed μ_a variations zones. Unaffected strand zones maintain the original coefficient of friction configuration (μ_a = 0.5 for aluminum-aluminum and aluminum-steel contacts). The steel-steel contact coefficients of friction are fixed at μ_a = 0.3 throughout.

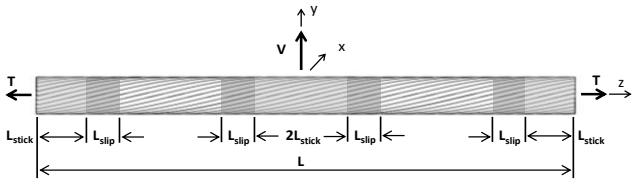

Fig. 16 - Two-level coefficient of friction model configuration

In addition, in order to extend the description of the multi-level coefficient concept, extreme values for μ_a of 0.9 and 0.1 are also evaluated in the stick and sliding zones of the aluminum-aluminum and aluminum-steel contacts. Fig. 17 reproduces the result of Fig. 9 and adds the deflection and hysteresis predictions established for the two aforementioned configurations, introducing variable μ_a.

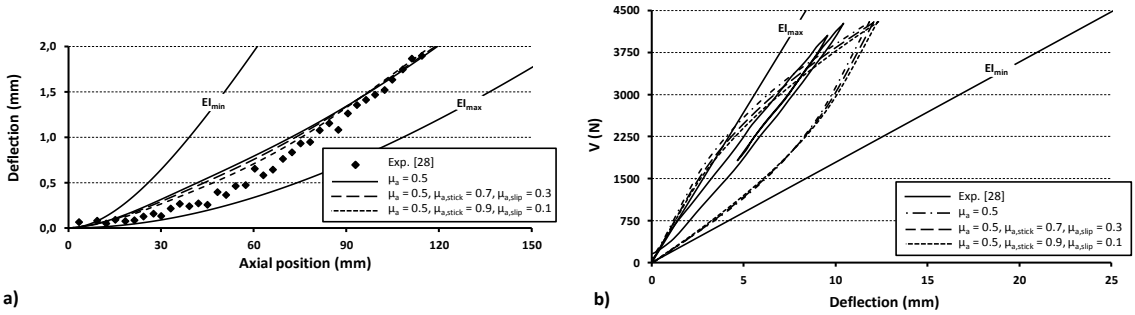

Fig. 17 - ACSR Cardinal (T = 40 kN and V_{max} = 4.3 kN), (a) deflection and (b) load-deflection curve at the cable center (z = 0 mm) V variation between 0 and V_{max} considering multi-level μ_a

The curves in the chart of Fig. 17a) show some precision gains realized with the multi-level adhesion coefficient of friction; the predicted deflection better represents experimental data. However, the approach does not significantly influence the friction dissipation; even with the overemphasis brought in with the 0.9 and 0.1 coefficient values, the numerical hysteresis curves presented in Fig. 17b) remain practically unchanged. Therefore, it must be concluded that the multi-zone adhesion coefficient of friction shown in Fig. 16 is not sufficient to explain the experimental observations.

5.3 Orthogonal friction coefficient effect

The previous evaluations only considered the adhesion contribution to friction or $\mu = \mu_a$. The obtained results tend to indicate that this approach is too simplistic, and that a more realistic formulation should incorporate the deformation process. The coefficient of friction (μ) should hence be written as: $\mu = \mu_a + \mu_d$, where μ_d represents the deformation contribution. Fig. 18(a) shows typical local alterations of wire surfaces caused by contact loads. In addition to adhesion phenomena described by μ_a, this type of plastic deformation may mechanically constrain the relative displacements of the wires. However, since the proposed FE model does not account for wire cross-section alterations, the deformation contribution cannot be directly integrated. On the other hand, the above μ formulation can easily compensate for this aspect and embody this additional constraint via μ_d. In reality, the indentation marks generated at the contact points plausibly promote inter-wire slip in a preferred direction.

The friction may be defined in orthogonal directions corresponding to the strand axial direction (Direction 1) and the direction (Direction 2) resulting from the cross product between Direction 1 and the normal to the radial contact point (Fig. 18b). Direction 1 and Direction 2 do not aim at defining an exact representation of the local indentation mark orientation, but rather, it is to provide a global representation of the strand assembly. The coefficients of friction μ_1 and μ_2 represent Directions 1 and 2, respectively. These coefficients are expressed as $\mu_i = \mu_{ai} + \mu_{di}$.

The expression of the coefficient of friction may be reduced to a unique function of μ_a: $\mu_i = \mu_{ai}(1+c_{di})$, where the constant c_{di} represents the deformation contribution. Moreover, considering $\mu_{a2} = \mu_{a1}$, the relation between μ_1 and μ_2 may be defined by the ratio $\mu_2/\mu_1 = (1+c_{d2})/(1+c_{d1})$. As well, assuming that Direction 1 is controlled by adhesive bonds, c_{d1} may be set to zero. The μ_2/μ_1 value is then reduced to $(1 + c_{d2})$.

In the model, μ_1 and μ_2 are independent parameters. Hence, setting μ_2 to zero would isolate the adhesion contribution, whereas setting μ_1 to zero would emphasize the friction caused by the deformations.

To illustrate the influence of the orthogonal friction concept, the following section re-evaluates the ACSR Cardinal response when c_{d2} is set to 0, 4, 9 and 14, which leads to the corresponding μ_2/μ_1 ratios 1, 5, 10 and 15, respectively. Fig. 19 presents the simulation results established for these ratios when the aluminum-aluminum μ_a values are 0.5, 0.7 and 0.9. The coefficients of friction at the steel-steel and steel-aluminum contacts were maintained at 0.3 and 0.5, respectively.

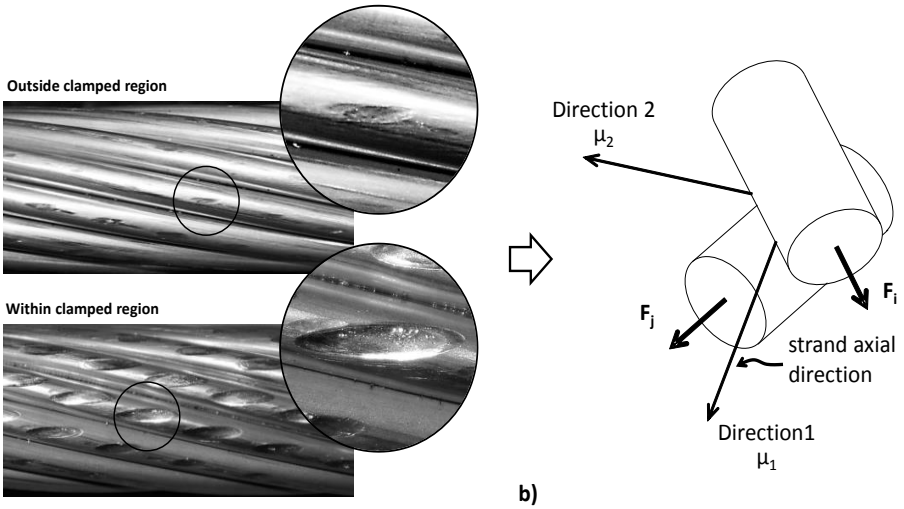

a) b)

Fig. 18 - (a) Indentation marks at inter-wire contact interfaces between layers 3 and 4 of a 19/54 ACSR Géant after being submitted to an axial tension of 20% RTS and (b) their interpretation with orthogonal friction coefficient concept

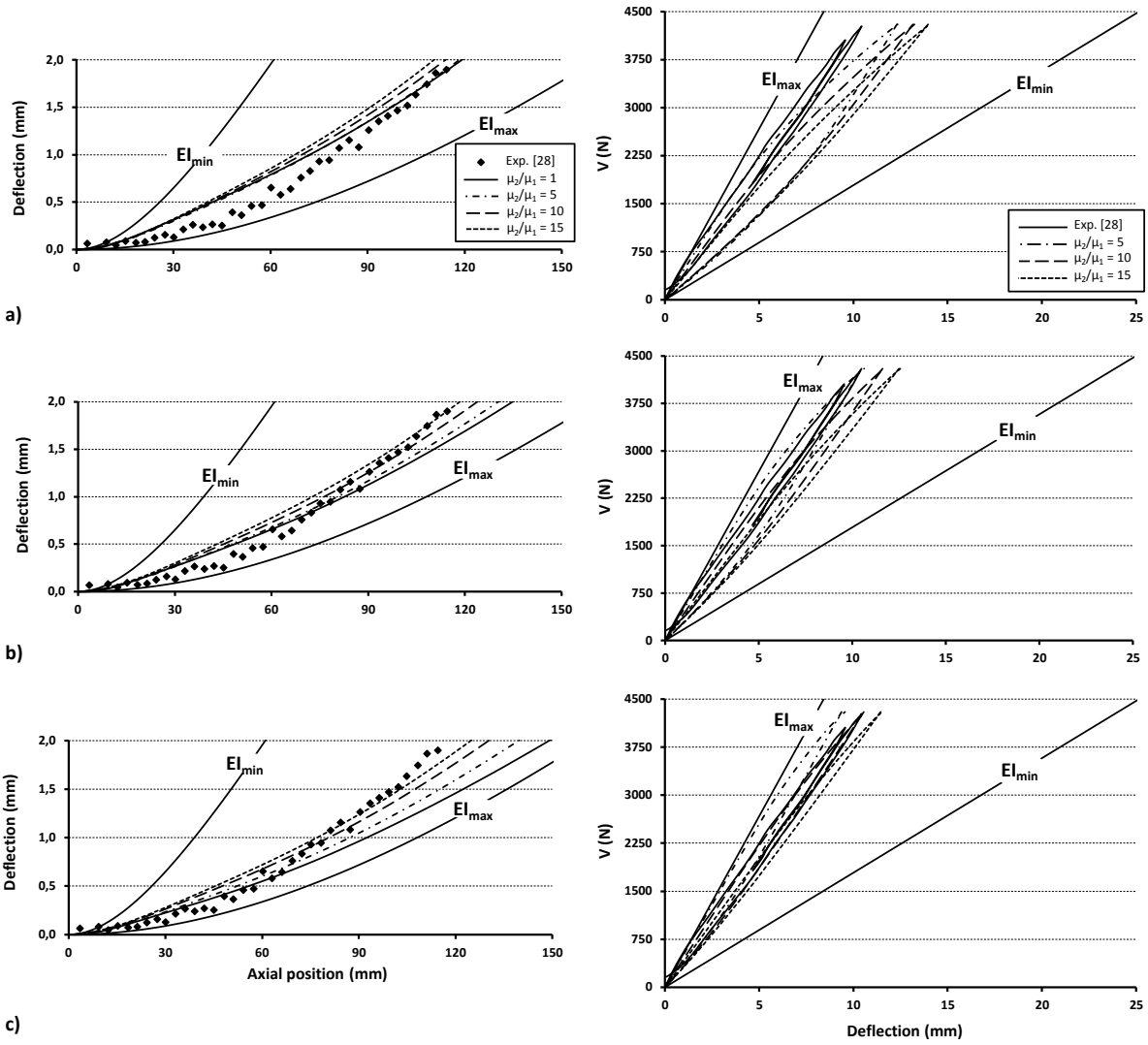

Fig. 19 - ACSR Cardinal (T = 40 kN and V_{max} = 4.3kN), deflection (left) and load-deflection curves at the cable center (z = 0 mm) (right), considering orthogonal friction coefficients with a) μ_a = 0.5, b) μ_a = 0.7 and c) μ_a = 0.9

The results shown in Fig. 19 indicate that the orthogonal concept influences the deflection behavior. Fig. 19b (μ_a = 0.7) presents the best predictions. On the other hand, the hysteresis curves also given in Fig. 19 support the hypothesis of a preferred inter-wire slip direction. Indeed, the introduction of an orthogonal friction model considerably reduces the load/deflection hysteresis area, and the numerical results better compare with the reported experimental values.

The graphs in Fig. 19 show that the effects of the orthogonal model improve with μ_a augmentations: while Fig. 19(a) still displays hysteresis areas larger and rigidities lower than measurements, Fig. 19(b) and (c) show responses closer to the experimental data.

The results of Fig. 19 may be summarized as follows:

1. Increasing μ_a (or μ_1) increases the Bending Stiffness (EI), and decreases the Hysteresis Area (HA);

2. Increasing μ_2/μ_1 decreases both EI and HA.

On the one hand, when only considering HA, Fig. 19 shows that the best predictions should be obtained with a ratio μ_2/μ_1 > 15 when μ_a = 0.5, with a μ_2/μ_1 ratio between 10 and 15 or around 12.5 when μ_a = 0.7, and when μ_a = 0.9 the optimal solution is at μ_2/μ_1 = 10. On the other hand, when considering EI and HA, Fig. 19 indicates that the best response is obtained with a ratio μ_2/μ_1 of 5 when μ_a = 0.5 or 0.7, while with μ_a = 0.9, the best ratio remains μ_2/μ_1 = 10.

Clearly, the above observations describe opposing trends. Nevertheless, as expected, the evaluations suggest that μ_1 and μ_2 virtually describe dependent contributions. And since the best solution should account for both EI and HA, considering the limited number of numerical evaluations and the absence of experimental measurements in the literature, the best evaluation remains μ_2/μ_1 around 5.5 and 10 for μ_a = 0.5, 0.7 and = 0.9, respectively.

Considering Fig. 19(b), which indicates that the best correspondence with the experimental measures is obtained with μ_a = 0.7, and assuming that $\mu_1 = \mu_a$, the previous results suggest that, when considering constant orthogonal coefficients of friction along the modeled strand, the best evaluations should be obtained with μ_a = 0.7 and μ_2 = 3.5 (c_{d2} = 4)

5.4 Orthogonal variable adhesion friction coefficient

The previous sections demonstrated that: 1. the deflection amplitude is affected by the coefficient of friction distribution along the strand, as well as by the orthogonal concept, and 2. the hysteresis response remains practically unaffected by lengthwise variations of the coefficient of friction, but are largely influenced by the orthogonal concept. Since both coefficient of friction descriptions reflect physical aspects of the strand tribological conditions, this section evaluates the amalgamation of the two representations.

Based on the observations of Sections 5.1 to 5.3, the next simulations evaluate the response quality obtained with the following friction parameter values: μ_a = 0.1, 0.9 and 0.7 in the slip, stick and unaffected zones defined in Fig. 16, respectively; μ_2 is set to 3.5 at all aluminum-aluminum contacts, while the steel-steel and aluminum-steel contact coefficients of friction remain fixed at μ_a = 0.3 and 0.5, respectively. Furthermore, to illustrate the influence of μ_2 on the global representation, the following evaluations also test the previous parameters setting when only μ_2 is changed to 2.

Fig. 20 compares the obtained results with the experimental measures. The graph also includes the initial solution of Fig. 9.

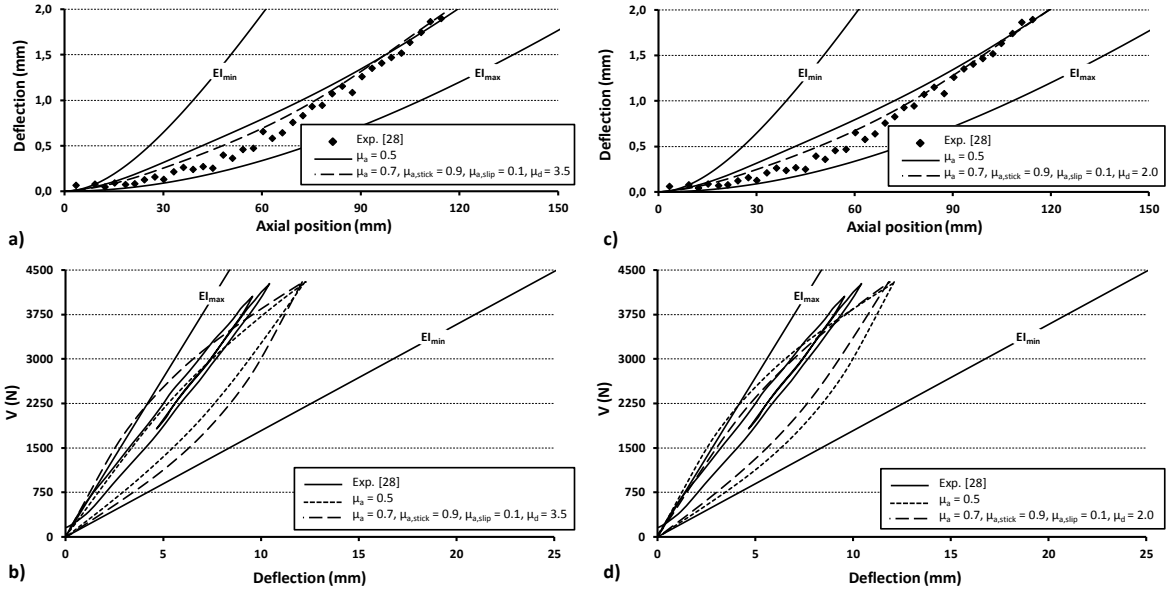

Fig. 20 - ACSR Cardinal (T = 40 kN & V_{max} = 4.3 kN), (a and c) deflection V = Vmax and (b and d) load-deflection curve at the cable center (z = 0 mm) V variations between 0 and Vmax considering multi-level and orthogonal coefficient concepts with μ_2 values 3.5 and 2.0

Fig. 20 demonstrates the improvement in quality of the solution resulting from the combination of the two concepts (orthogonality and lengthwise variations). The deflection curves established for V_{max} shown in Fig. 20(a) and (c) now better correspond to the experimental measures.

On the other hand, although the results presented in Fig. 17 indicate that μ_a lengthwise variations should have no significant influence on HA, the evaluations shown in Fig. 20(b) and (d) reveal that, when associated with the orthogonality concept, additional internal interactions take place, reduce the overall conductor EI, and increase HA. Therefore, for an optimal fit to the experimental data, adjustment iterations would be required. However, since the objective here is not to establish a perfect match, but rather, to illustrate the influence of the proposed concept on the model response, the last fine tuning operations are not included. On the other hand, the conclusions drawn in Section 5.3 from Fig. 19 remain valid; compared to μ_2 = 3.5, μ_2 = 2.0 increases EI and HA.

The last test illustrates the influence of the axial coefficient of friction value at the aluminum-steel contacts. The results shown in Fig. 21 reproduce the simulations presented in Fig. 20(a) and (c) when the aluminum-steel contact coefficient of friction is changed from μ_1 = 0.5 to 0.7. Fig. 21 also includes the Fig. 20 evaluations. While Fig. 21a displays practically unchanged values, Fig. 21b indicates that increasing μ_1 at all aluminum wire contact points further reduces HA, and slightly increases EI. Even though all coefficient of friction values examined in this investigation remain in agreement with published experimental measurements, this last setting demonstrates the best correspondence with the global strand response.

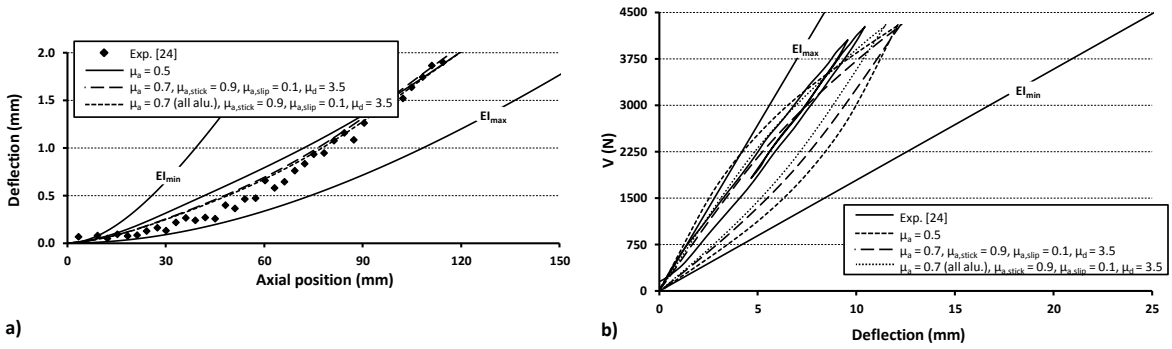

Fig. 21 - ACSR Cardinal (T = 40 kN and V_{max} = 4.3 kN), (a) deflection V = Vmax and (b) load-deflection curve at the cable center (z = 0 mm) V variation between 0 and Vmax considering multi-level and orthogonal coefficient concepts with μ_2 values 3.5 and μ_a = 0.7 everywhere

5. Conclusion

This paper proposed a FE modeling strategy for multilayered strands subjected to multiaxial loads. Although taking advantage of second-order beam elements, the approach also incorporates all 3D inter-wire contact types. Therefore, while avoiding the simplification inherent to published analytical formulations, and drastically reducing the mesh size compared to other numerical modeling procedures, the proposed strategy can handle any strand geometry-load configurations, and deals with large deformations.

Comparisons to experimental and full 3D FE results demonstrate the precision of the proposed procedure at both global strand displacement and interlayer contact force transmission levels. A comparison to the experimental work published by Papailiou for combined axial/bending loads illustrated the capacity of the approach to reproduce the load/deflection hysteresis under cyclic bending loads.

The analysis showed that the friction forces control the load/deflection hysteresis as well as the global conductor bending stiffness. In order to account for the influence of the wire internal forces on contact force distributions, contact areas, and ultimately, on the adhesive coefficient of frictions μ_a, a multi-level friction coefficient better representing the stick and slip zone distributions was introduced. The lengthwise coefficient variations demonstrated visible effects on the strand deflection, but no significant influence on the hysteresis response. The experimental hysteresis measures published by Papailiou were then indirectly assumed to be potentially affected by indentation marks at the aluminum contact points. These marks were assumed to alter the friction forces.

To account for possible indentation marks at the aluminum contact points, the friction orthogonality concept was incorporated into the model. This approach was shown to have a considerable influence on the hysteresis response; an increase of the coefficient of friction in the axial direction of the strand augments the bending stiffness and decreases the

hysteresis area, whereas an increase of contribution of the coefficient of friction in orthogonal directions decreases both the bending stiffness and the hysteresis area. The analysis described the axial direction as mainly controlled by adhesive forces ($\mu_1 = \mu_a$), while the orthogonal directions are associated with adhesion combined with dominant deformation (μ_d) contributions or $\mu_2 = \mu_a + \mu_d$.

A combination of the lengthwise variations of the coefficient of friction and the friction orthogonality concept provided a significant improvement of the predictions. For example, although the analysis only aimed to establish the procedure, and did not intend to match the reference data with a perfect correspondence, the best agreement with experimental measurements published for an ACSR Cardinal strand were obtained with $\mu_1 = \mu_a = 0.7$ and $\mu_2 = 3.5$.

The proposed modeling strategy offers insights into internal element variations of multilayered strands, and since it allows precise 3D simulations of strand segments of several pitch lengths using modest computational resources, it certainly represents a powerful design tool.

Acknowledgments

This research project was funded by the Natural Sciences and Engineering Research Council (NSERC) of Canada and the Hydro-Quebec/RTE - Structure and mechanics of power transmission lines research chair at Sherbrooke University.

References

[1] Fricke W.G. J, Rawlins CB. Importance of fretting in vibration failures of stranded conductors. IEEE Trans Power Appar Syst 1968;PAS-87:1381–4.
[2] Raoof M, Davies TJ. End fixity to spiral strands undergoing cyclic bending. J Strain Anal Eng Des 2005;40:129–37.
[3] Cardou A, Jolicoeur C. Mechanical models of helical strands. Appl Mech Rev 1997;50:1–14.
[4] Raoof M, Hobbs RE. Bending of spiral strand and armored cables close to terminations. J Energy Resour Technol Trans ASME 1984;106:349–55.
[5] Lanteigne J. Theoretical estimation of the response of helically armored cables to tension, torsion, and bending. J Appl Mech Trans ASME 1985;52:423–32.
[6] LeClair RA, Costello GA. Axial, bending and torsional loading of a strand with friction. J Offshore Mech Arct Eng 1988;110:38–42.
[7] Argatov I. Response of a wire rope strand to axial and torsional loads: Asymptotic modeling of the effect of interwire contact deformations. Int J Solids Struct 2011;48:1413–23. doi:10.1016/j.ijsolstr.2011.01.021.
[8] Frikha A, Cartraud P, Treyssède F. Mechanical modeling of helical structures accounting for translational invariance. Part 1: Static behavior. Int J Solids Struct 2013;50:1373–82. doi:10.1016/j.ijsolstr.2013.01.010.
[9] EPRI. EPRI Transmission line reference book: Wind-induced conductor motion. Palo Alto, CA: 2006.
[10] Papailiou KO. On the bending stiffness of transmission line conductors. IEEE Trans Power Deliv 1997;12:1576–83.
[11] Hong K-J, Kiureghian A Der, Sackman JL. Bending behavior of helically wrapped cables. J Eng Mech 2005;131:500–11. doi:10.1061/(ASCE)0733-9399(2005)131:5(500).
[12] Paradis J-P, Legeron F. Modelling of the free bending behavior of a multilayer cable taking into account the tangential compliance of contact interfaces. Cable Dyn., 2010.

[13] Cardou A. Taut helical strand bending stiffness. UFTscience 2006.
[14] Judge R, Yang Z, Jones SW, Beattie G. Full 3D finite element modelling of spiral strand cables. Constr Build Mater 2012;35:452–9.
[15] Shibu G, Mohankumar K V, Devendiran S. Analysis of a three layered straight wire rope strand using finite element method. Proc. World Congr. Eng. 2011, WCE 2011, vol. 3, 2011, p. 2588–93.
[16] Stanova E, Fedorko G, Fabian M, Kmet S. Computer modelling of wire strands and ropes Part I: Theory and computer implementation. Adv Eng Softw 2011;42:305–15.
[17] Frigerio M, Buehlmann PB, Buchheim J, Holdsworth SR, Dinser S, Franck CM, et al. Analysis of the tensile response of a stranded conductor using a 3D finite element model 2016;106:176–83. doi:10.1016/j.ijmecsci.2015.12.015.
[18] Stanova E, Fedorko G, Fabian M, Kmet S. Computer modelling of wire strands and ropes part II: Finite element-based applications. Adv Eng Softw 2011;42:322–31.
[19] Zhang D, Ostoja-Starzewski M. Finite Element Solutions to the Bending Stiffness of a Single-Layered Helically Wound Cable With Internal Friction. J Appl Mech 2015;83:031003. doi:10.1115/1.4032023.
[20] Beleznai R, Páczelt I. Design curve determination for two-layered wire rope strand using p-version finite element code. Eng Comput 2013;29:273–85.
[21] Zhou W, Tian H-Q. A novel finite element model for single-layered wire strand. J Cent South Univ 2013;20:1767–71.
[22] Ghoreishi SR, Messager T, Cartraud P, Davies P. Validity and limitations of linear analytical models for steel wire strands under axial loading, using a 3D FE model. Int J Mech Sci 2007;49:1251–61.
[23] Kumar K, Botsis J. Contact stresses in multilayered strands under tension and torsion. Trans ASME J Appl Mech 2001;68:432–40.
[24] Raoof M, Huang YP. Wire stress calculations in helical strands undergoing bending. J Offshore Mech Arct Eng 1992;114:212–9.
[25] Utting WS, Jones N. The response of wire rope strands to axial tensile loads-Part I. Experimental results and theoretical predictions. Int J Mech Sci 1987;29:605–19.
[26] Jiang WG, Henshall JL. Analysis of termination effects in wire strand using the finite element method. J Strain Anal Eng Des 1999;34:31–8.
[27] Judge RP. Structural cables subjected to blast fragmentation. University of Liverpool, 2012.
[28] Papailiou KO. Bending of helically twisted cables under variable bending stiffness due to internal friction, tensile force and cable curvature. Swiss Federal Institute of Technology in Zurich, 1995.
[29] Monroe RA, Templin RL. Vibration of overhead transmission lines. Am. Inst. Electr. Eng. -- Meet., New York, NY, United States: American Institute of Electrical Engineers; 1932, p. 15.
[30] Levesque F, Goudreau S, Langlois S, Legeron F. Experimental Study of Dynamic Bending Stiffness of ACSR Overhead Conductors. IEEE Trans Power Deliv 2015;30:2252–9. doi:10.1109/TPWRD.2015.2424291.
[31] Wharton MH, Waterhouse RB, Hirakawa K, Nishioka K. The effect of different contact materials on the fretting fatigue strength of an aluminium alloy. Wear 1973;26:253–60. doi:10.1016/0043-1648(73)90139-7.
[32] Azevedo CRF, Henriques AMD, Pulino Filho AR, Ferreira JLA, Araújo JA. Fretting fatigue in overhead conductors: Rig design and failure analysis of a Grosbeak aluminium cable steel reinforced conductor. Eng Fail Anal 2009;16:136–51. doi:10.1016/j.engfailanal.2008.01.003.